Chapter 3

Computational Results and Discussions

3.1 Computation background

The dynamics of the current sheath during the axial acceleration phase is modelled based on the Snow-plow model. The equation of motion is

$$\frac{d^2z}{dt^2} = \frac{\left[\frac{{f_c}^2}{f_m}\frac{\mu_0(lnc)}{4\pi^2\rho_0(c^2-1)}\left(\frac{I}{a}\right)^2 - \left(\frac{dz}{dt}\right)^2\right]}{z} \quad \ldots\ldots (3.1)$$

Where z is the axial position, ρ_0 is the ambient gas density, μ_0 is the permeability of free space ($4\pi\times10^{-7}$ Hm^{-1}), c is $\left(b/a\right)$, b is the radius of the outer electrode, a is the radius of the inner electrode, I is the coaxial discharge current, f_m is the fraction of mass swept down the tube in the z-direction and f_c is the fraction of current flowing in the piston.

The coupled circuit equation is written as

$$\frac{dI}{dt} = \frac{V_0 - \frac{\int Idt}{C_0} - \frac{\mu_0}{2\pi}ln(c)\,If_c\frac{dz}{dt}}{L_0 + \frac{\mu_0 f_c}{2\pi}ln(c)\,z} \quad \ldots\ldots (3.2)$$

Both Equation (3.1) and (3.2) are normalized to give

$$\frac{d^2\zeta}{d\tau^2} = \frac{\alpha^2\iota^2 - \left(\frac{d\zeta}{d\tau}\right)^2}{\zeta} \quad \ldots\ldots (3.3)$$

and

$$\frac{d\iota}{d\tau} = \frac{1 - \int \iota d\tau - \iota\beta\frac{d\zeta}{d\tau}}{1+\beta\zeta} \quad \ldots\ldots (3.4)$$

The normalized Equations (3.3) and (3.4) are solved simultaneously and integrated by using the Euler's method with the following initial conditions:

$$\tau = 0, \qquad \zeta = 0, \qquad \frac{d\zeta}{d\tau} = 0, \qquad \frac{d^2\zeta}{d\tau^2} \xrightarrow{\tau \to 0} \frac{\alpha}{\sqrt{2}}, \quad \iota = 0, \qquad \int \iota d\tau = 0, \quad \frac{d\iota}{d\tau} = 1$$

3.2 Computational result

The axial acceleration phase of the 600 J Mather type plasma focus device is computed. The following operational parameters are used:

Energy bank capacity	C_0 = 3.7 μF
Charging voltage	V_0 = 18kV
Maximum stored energy	600 J
Inductance of circuit	L_0 = 130 nH
Impedance	$Z_0 = \sqrt{L_0/C_0}$ = 0.1874 Ω
Circuit resistance	25 mΩ
Maximum current	I_0 = 95.844 kA
Operating gas	Argon
Operating gas pressure	9.0×10^{-3} mbar – 1.8×10^{-2} mbar
Anode length	z_0 = 60 mm
Inner electrode (anode) radius	a = 4.75 mm
Outer electrode (cathode) radius	b = 23.75 mm

The density of the argon gas at room temperature is calculated by using the ideal gas law,

$$\rho = \frac{PM}{RT}$$

that ρ represents the gas density of the argon gas filling the plasma focus device.

By substituting the above operational parameters into the normalized Equation (3.3) and Equation (3.4), the axial rundown time of the current sheath, t_a and the axial rundown speed, v_a can be obtained.

3.2.1 Computational result for axial phase

The calculation is done in Excel Spreadsheet and the computed axial rundown time and speed at various gas pressures are shown in Table 3.1. The computed results for pressure 9×10^{-3} mbar is plotted in Figure 3.1.

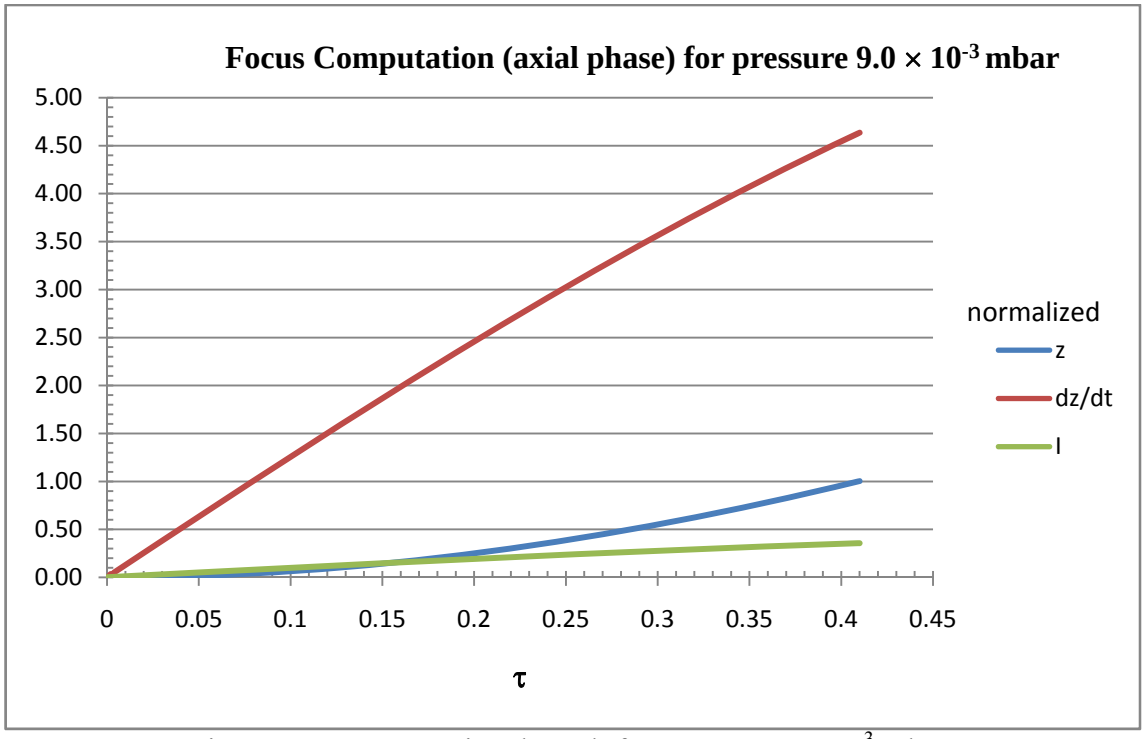

Figure 3.1: Computational result for pressure 9×10^{-3} mbar

The computation step starts at time zero and stops when the current sheath reaches the end of the electrodes. This is when the normalized axial position of the current sheath, ζ becomes 1. At pressure 9×10^{-3} mbar the results obtained show that the current sheath reaches the end of the electrode at τ=0.410, that the characteristics time t_a is 0.28 μs.

The average axial rundown speed, v_a can then be calculated from the total time spent in axial phase :

$$v_a = \frac{z_0}{t_a}$$

$$= \frac{6\ cm}{0.28\ \mu s}$$

$$\therefore v_a = 21.43\ cm\ \mu s^{-1}$$

Experiments have been carried out with argon gas, at various operating pressures range from 9×10^{-3} mbar to 1.8×10^{-2} mbar where prominent focusing action has been observed with good reproducibility and emission of x-ray and EUV have been obtained [Lee et al., 2010].

The discharge current has been measured and the typical signals are shown in Figure 3.2 (a) – (g). These typical signals allow us to identify the axial run down phase of the current sheath, where the rise of current sheath indicates its start and the current dip indicates it reaches the end of the electrode and collapses to form the plasma focus.

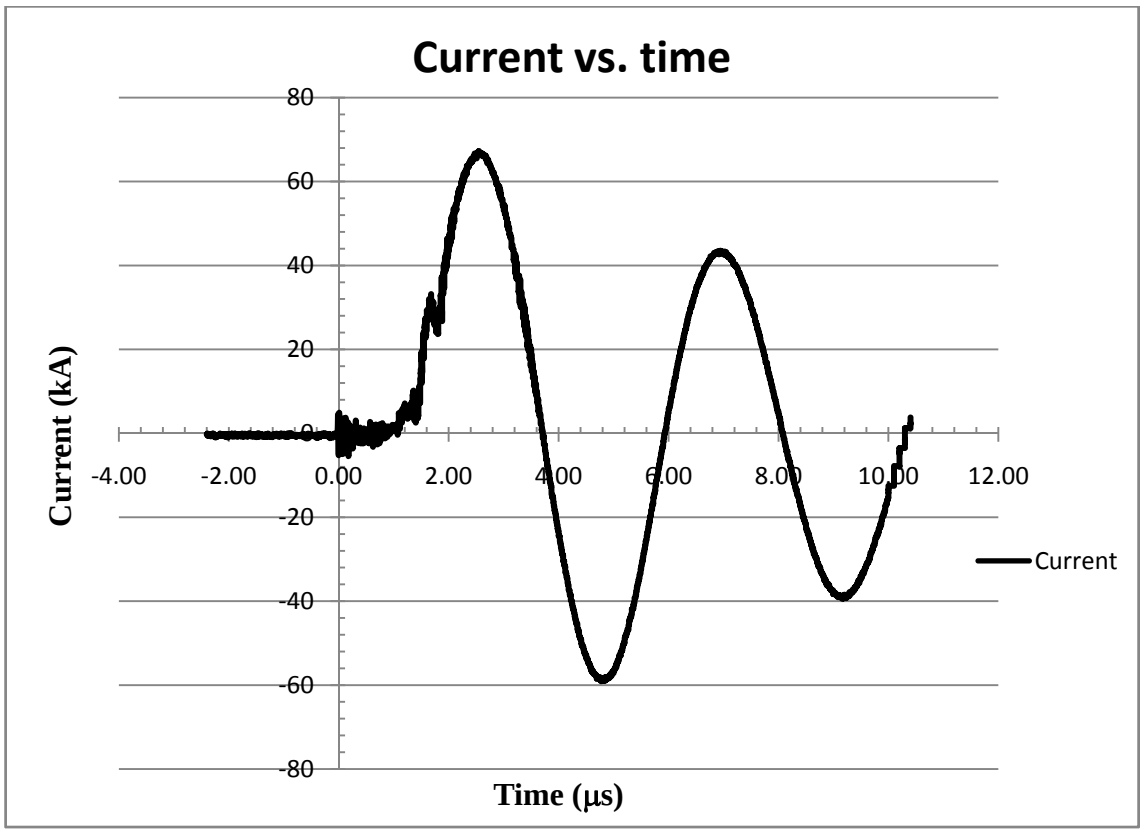

Figure 3.2 (a): Current trace for pressure at 9.0×10^{-3} mbar.

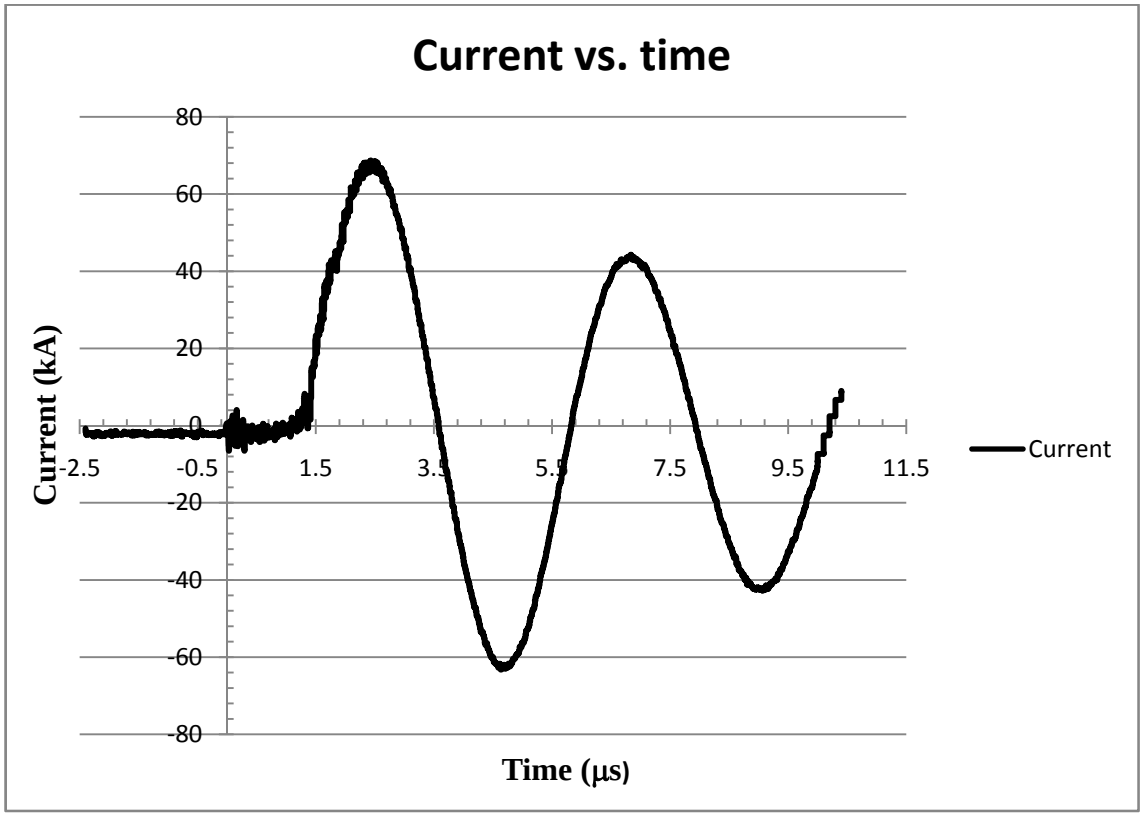

Figure 3.2 (b): Current trace for pressure at 1.0×10^{-2} mbar.

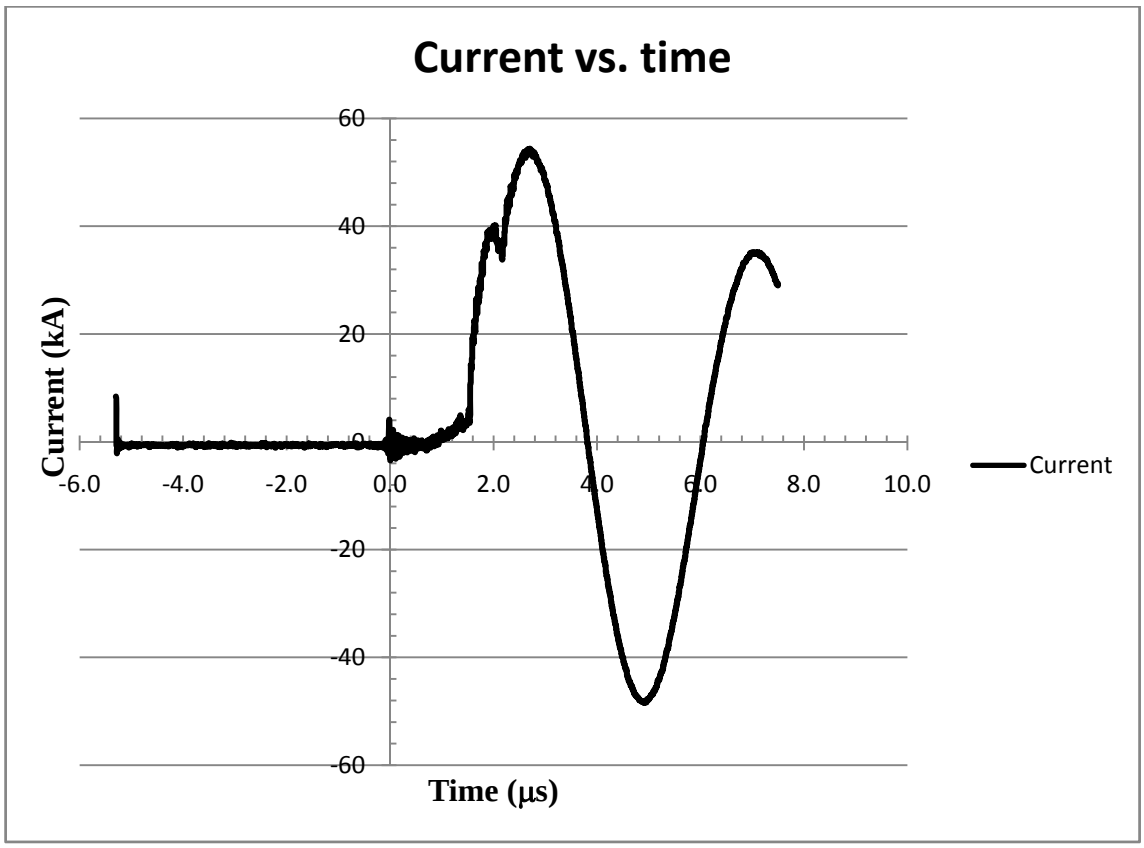

Figure 3.2 (c): Current trace for pressure at 1.4×10^{-2} mbar.

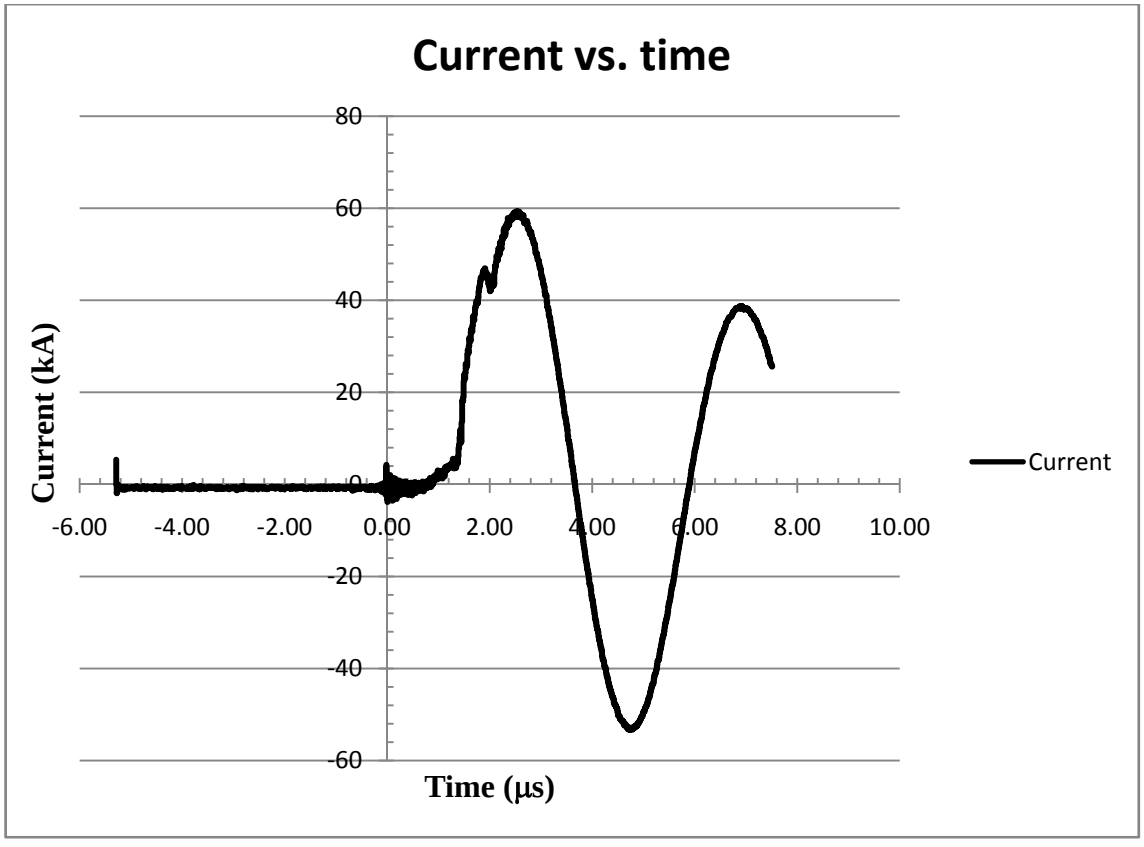

Figure 3.2 (d): Current trace for pressure at 1.5×10^{-2} mbar.

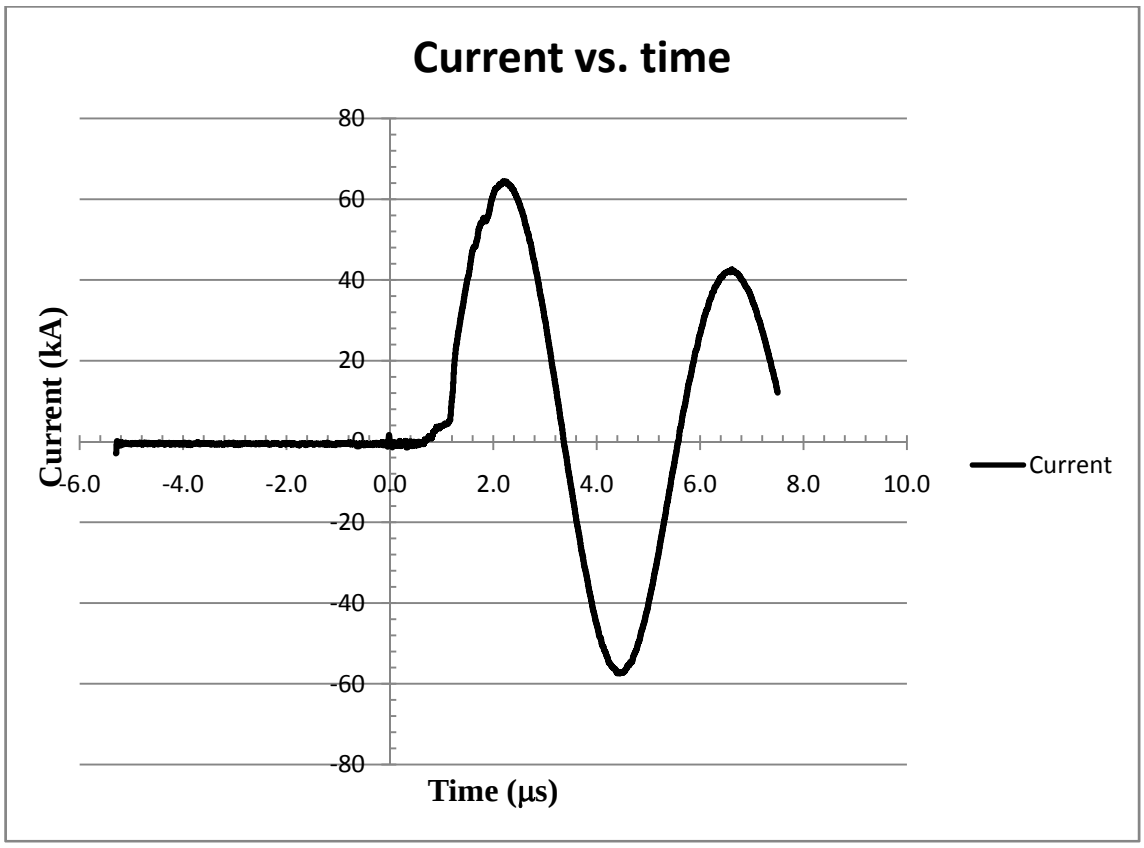

Figure 3.2 (e): Current trace for pressure at 1.6×10^{-2} mbar.

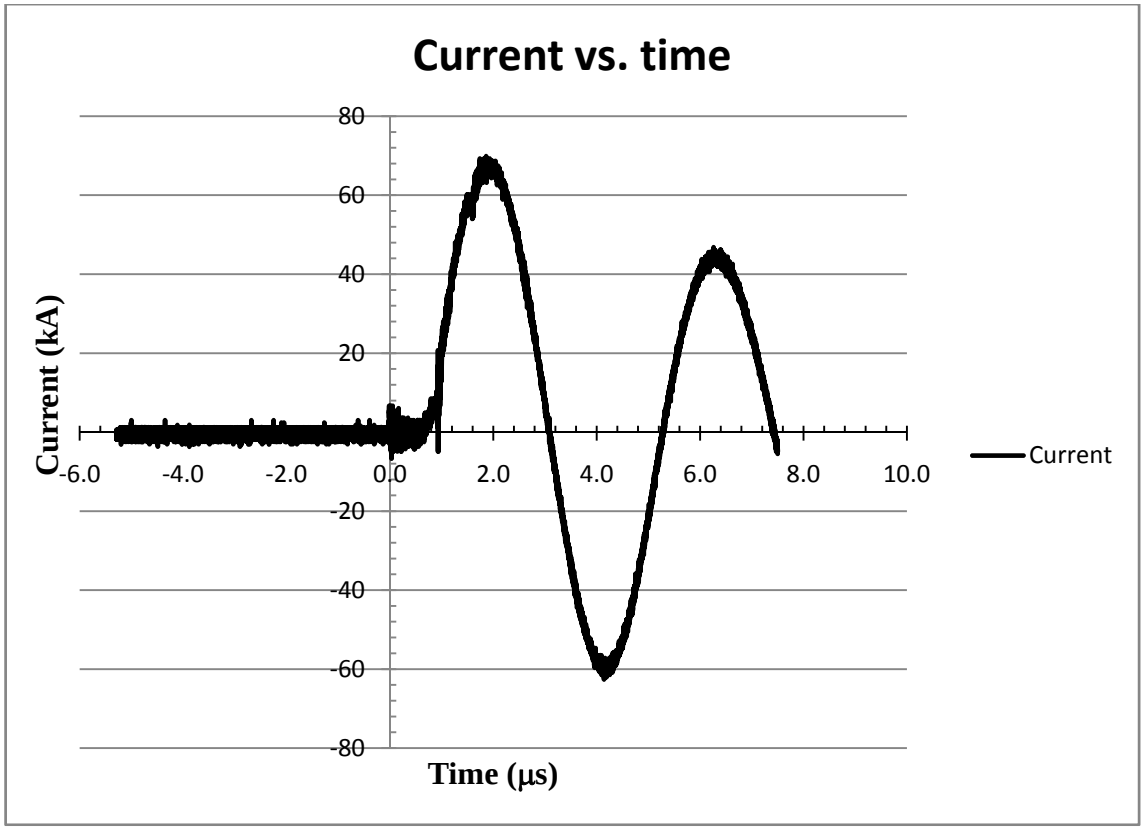

Figure 3.2 (f): Current trace for pressure at 1.8×10^{-2} mbar.

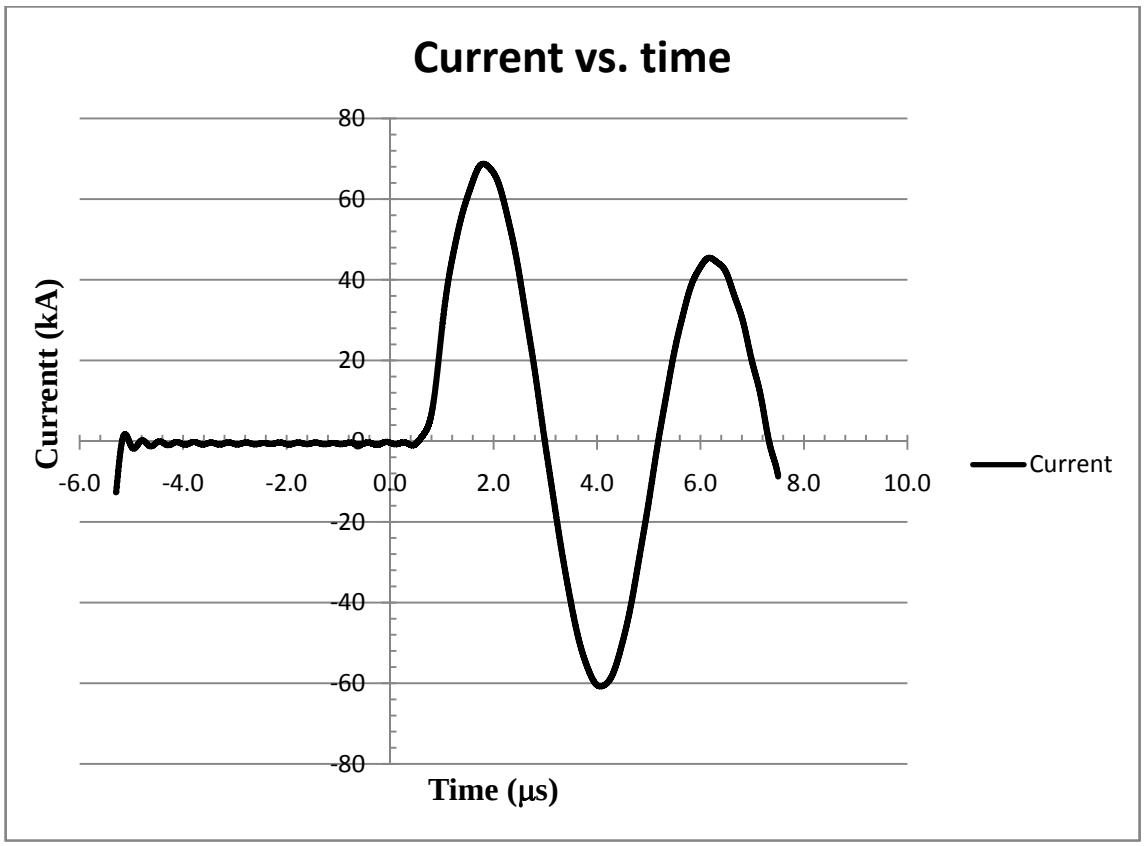

Figure 3.2 (g): Current trace for pressure at 2.0×10^{-2} mbar.

The discharge characteristic depends on the operating pressures. The beginning part of the current signal is more resistive at low pressure and the time of current dip is shorter at lower pressure. The axial phase is simulated with snow-plow model to match the duration of axial phase, which is from the current rise to the current dip. The computed results of the axial phase, which include the discharge current, the velocity of the current sheath and the position of the current sheath in axial phase for all the different operating pressures are shown in Figure 3.3 (a) – (e).

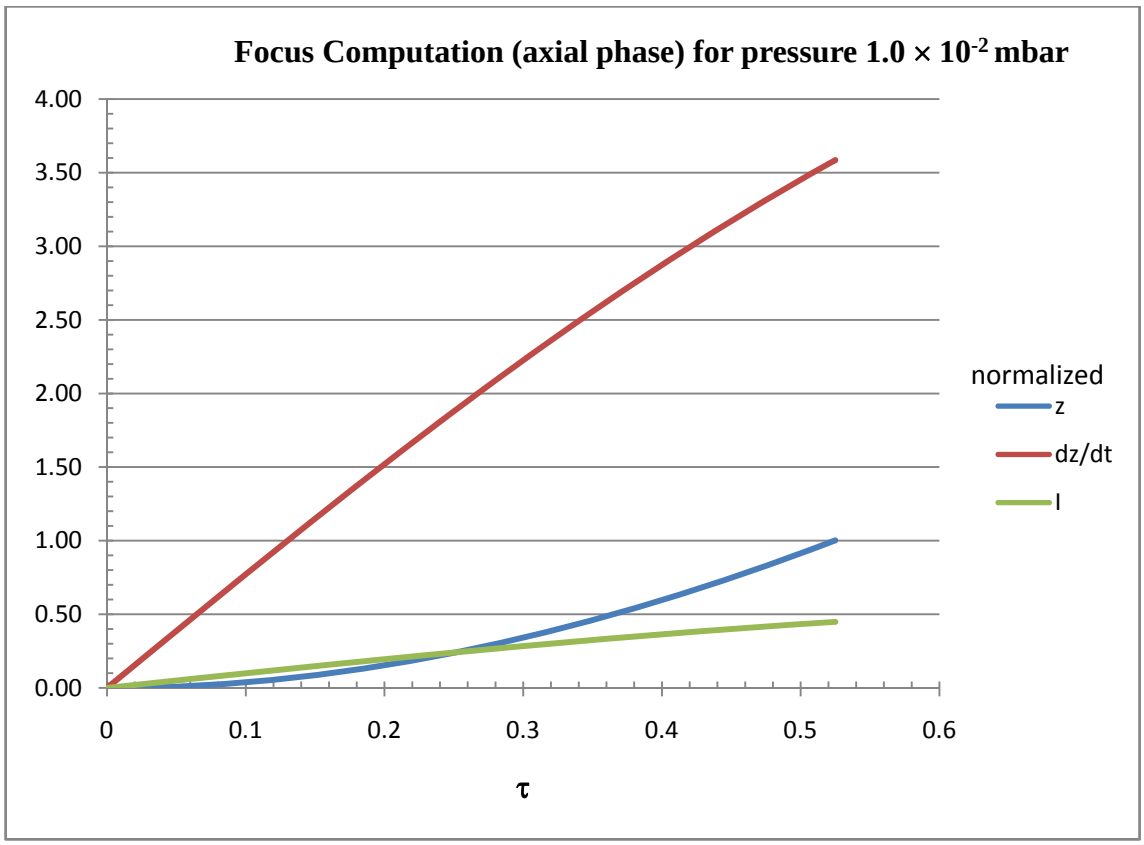

Figure 3.3 (a): Focus computation (axial phase) for pressure 1.0×10^{-2} mbar

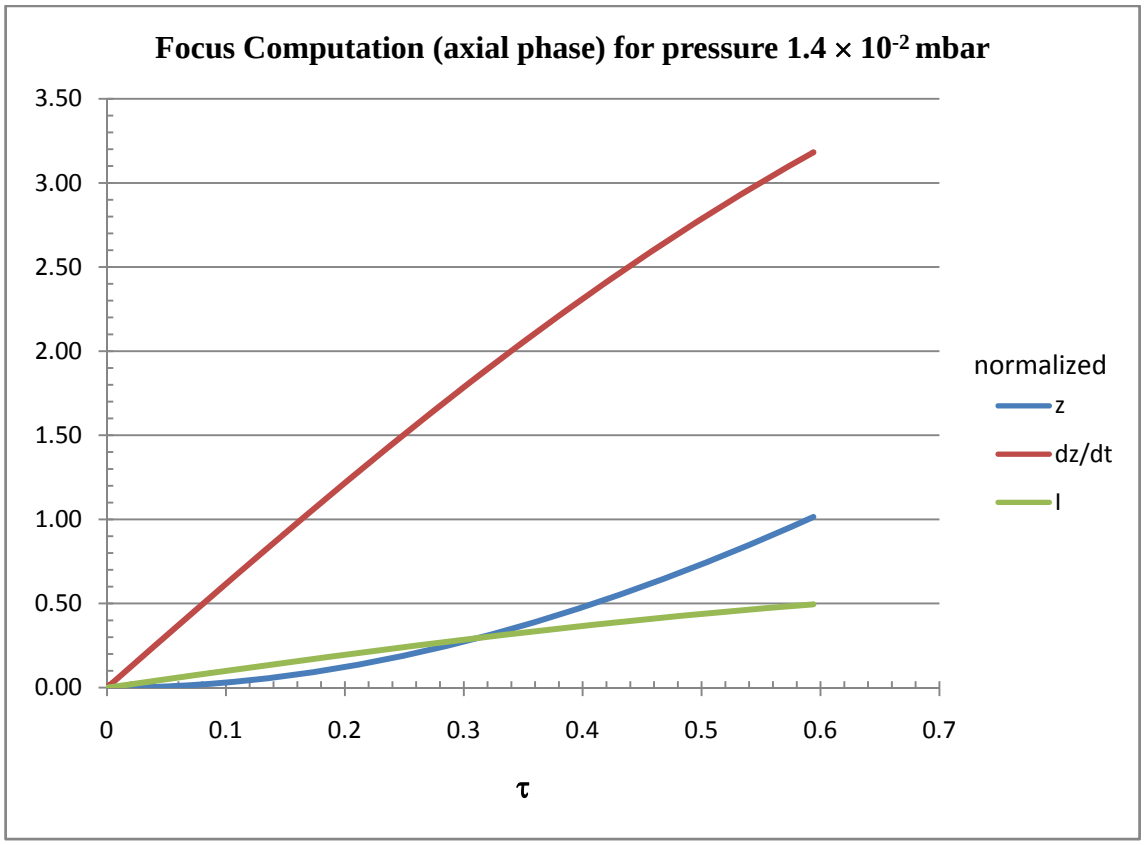

Figure 3.3 (b): Focus computation (axial phase) for pressure 1.4×10^{-2} mbar

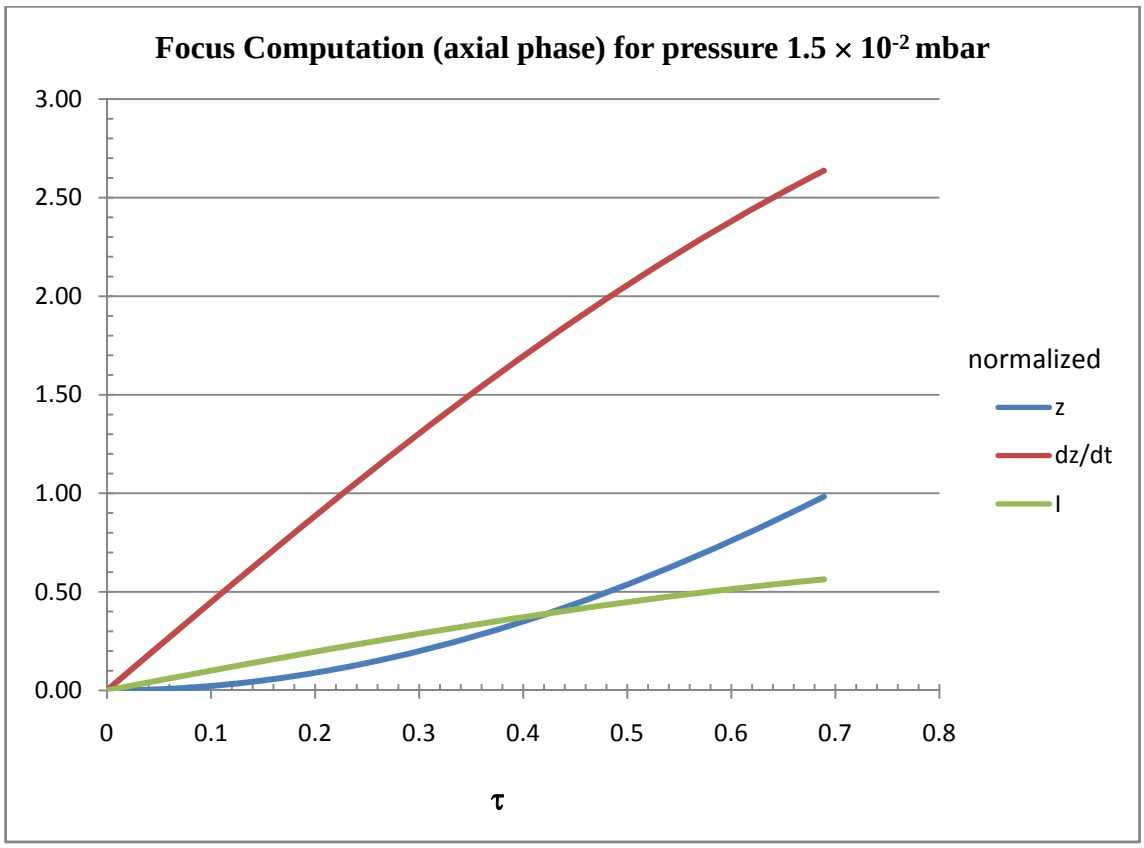

Figure 3.3 (c): Focus computation (axial phase) for pressure 1.5×10^{-2} mbar

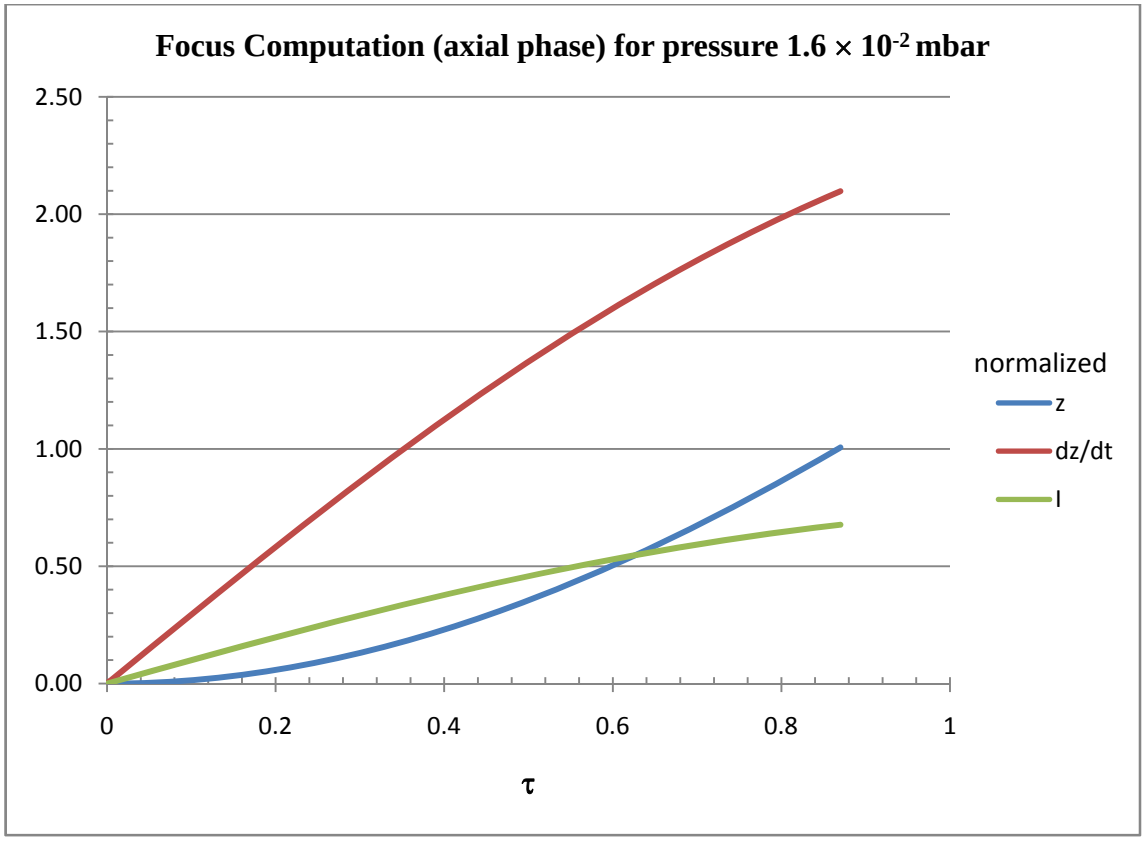

Figure 3.3 (d): Focus computation (axial phase) for pressure 1.6×10^{-2} mbar

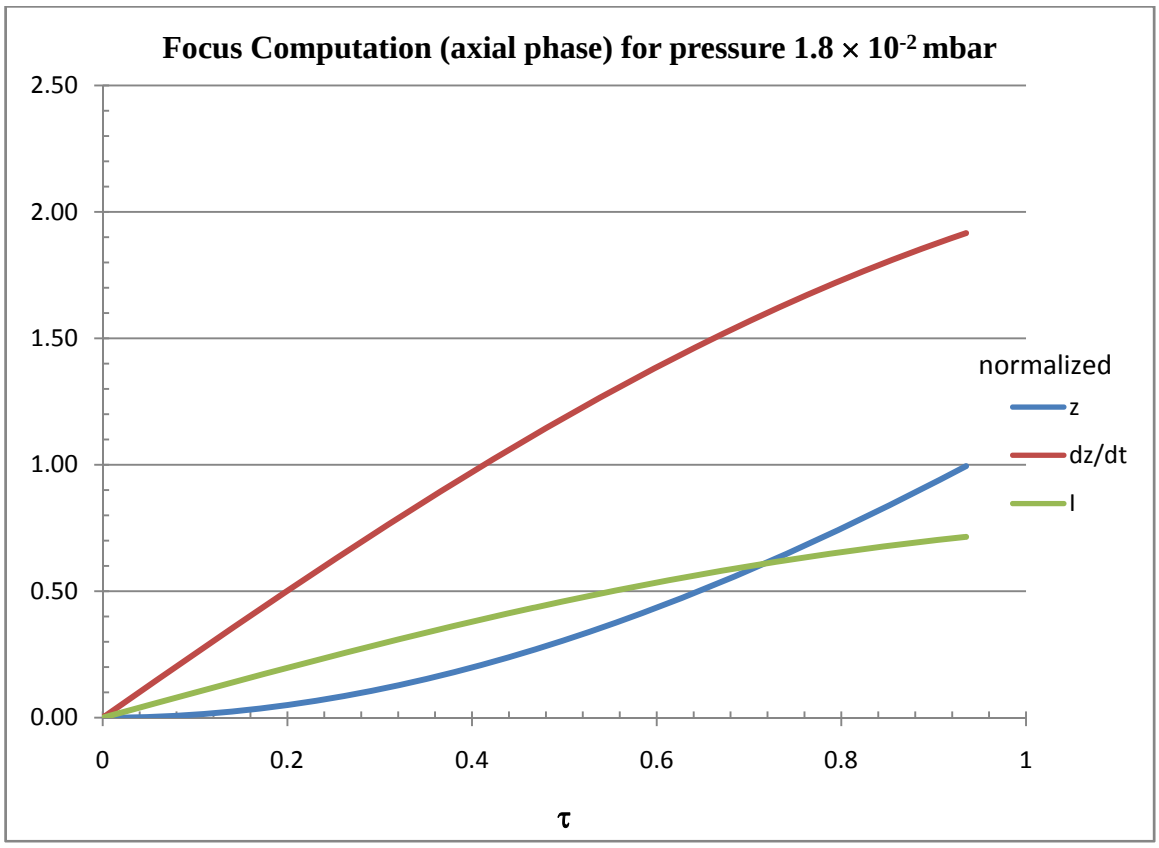

Figure 3.3 (e): Focus computation (axial phase) for pressure 1.8×10^{-2} mbar

The computation stops when current sheath reaches the end of the electrode, when $\zeta = 1$. The time register is the duration of the axial acceleration phase. The total time of axial acceleration phase and the respective average velocity for different pressures are summarized in Table 3.1:

Table 3.1: Computational result of the axial rundown time and speed at various gas pressures.

Filling gas pressure (mbar)	Normalized time, τ, when the current sheath reaches the end	Axial rundown time of the current sheath, $t_a = \tau \times t_0$ (μs)	Axial rundown speed of the current sheath, $v_a = \frac{z_0}{t_a}$ (cm μs^{-1})
9.0×10^{-3}	0.410	0.28	21.10
1.0×10^{-2}	0.525	0.36	16.48
1.4×10^{-2}	0.590	0.41	14.66
1.5×10^{-2}	0.696	0.48	12.43
1.6×10^{-2}	0.867	0.60	9.98
1.8×10^{-2}	0.938	0.65	9.22

Using the results shown in Table 3.1, a graph of current sheath axial speed versus gas pressure is plotted (Figure 3.4). It is depicted in the graph that for operating gas pressure that ranges between 9.0×10^{-3} mbar to 1.8×10^{-2} mbar, the estimated axial rundown speed falls within 9.22 cm μs^{-1} and 21.10 cm μs^{-1}. When the filling gas pressure is at 9.0×10^{-3} mbar, the axial rundown speed of the current sheath is the highest, which is 21.10 cm μs^{-1}. The experimental results also showed that stronger pinching was observed at lower pressure, which was indicated by the signals with higher voltage spike and larger current dip. On the other hand, from the computation, we also obtain the highest axial rundown speed, v_a of the current sheath when the operating gas pressure is at the lowest.

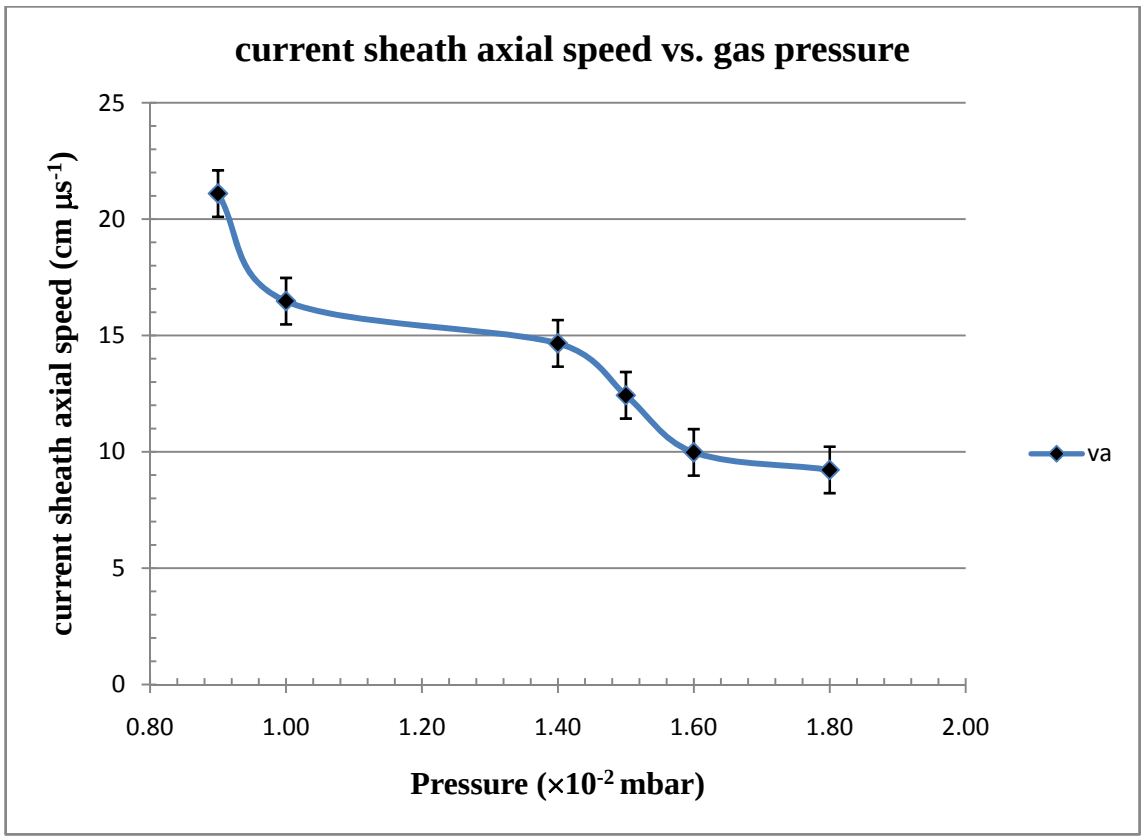

Figure 3.4: Graph of current sheath axial speed, v_a vs. gas pressure.

3.3 Comparison between computational results and experimental result

In order to reflect how realistic the computational results are, a comparison between a set of experimental results and the computational results are made and shown in Table 3.2 and Figure 3.5.

Table 3.2: Comparison between computational results and experimental results.

Operating gas pressure (mbar)	Experimental results for the time when focus is observed (μs)	Computational results when the current sheath reaches the end of the electrode (μs)
9.0×10^{-3}	0.27	0.28
1.0×10^{-2}	0.36	0.36
1.4×10^{-2}	0.41	0.41
1.5×10^{-2}	0.48	0.48
1.6×10^{-2}	0.59	0.60
1.8×10^{-2}	0.65	0.65

When the operating pressures are in the range of 9.0×10^{-3} mbar to 1.8×10^{-2} mbar, the computed axial rundown time is almost the same as the focus time observed experimentally, indicated by the voltage spike and current dip in the discharge signals. However, for pressure 2.0×10^{-2} mbar and above the discharge practically could not produce the plasma focus.

The simulated results are made as close to the experimental results as possible. It is necessary to assume that the current carried in the current sheath is a fraction of the external circuit current whilst the mass swept-up by the current sheath is a fraction of the total mass encountered in the axial phase. The two factors are referred to as current shedding and mass shedding factor. The matching of the simulated results to the experimental results has been achieved by selecting the suitable current shedding and

mass factors. For all the different operating pressures, the current shedding factor is varied between 0.8 and 0.9.

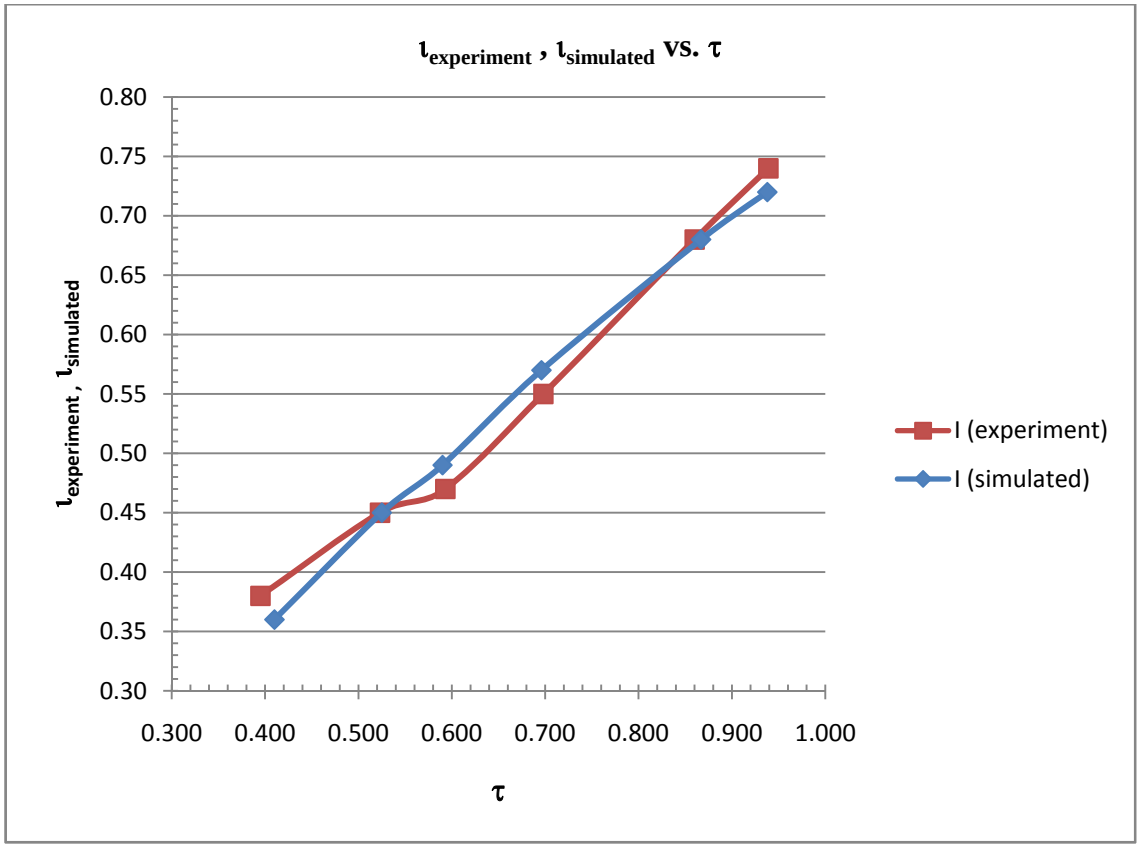

Figure 3.5: Graph of normalized current (experimental) and normalized current (simulated) vs. normalized time.

As the mass factor decreases at lower operating pressures, the speed increases. The mass factors between 0.018 and 0.34 are obtained for pressure 9.0×10^{-3} mbar to1.8×10^{-2} mbar. We can conclude from the computational results that the fraction of mass swept up is only about 1.8% to 34% of the total mass encountered, while the current that flows through the tube is about 80% - 90% of the external circuit current. The results are shown in Figure 3.6.

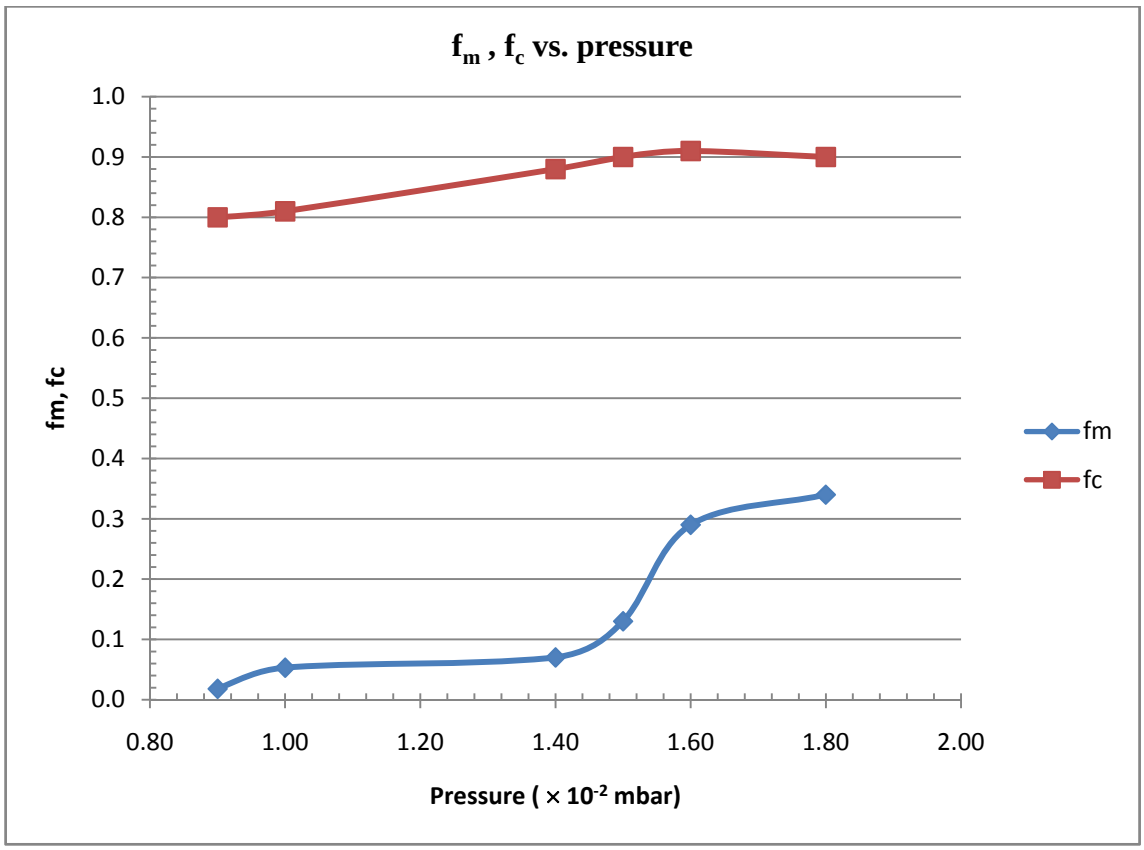

Figure 3.6: Graph of mass factor, f_m and current shedding factor, f_c vs. gas pressure

3.4 Calculation of plasma temperature

We can also determine from the computed results, the final speed of the current sheath when it reaches the end of the electrodes. From the simulated axial speed shown in Table 3.1 the axial speed values fall in the range of 9.22 cm μs^{-1} and 21.10 cm μs^{-1}. This shows that the speed of the current sheath (piston) has exceeded the supersonic speed (typically 0.0343 cm μs^{-1}) and could have been shock heated.

The shock front velocity v_{sf} can be obtained from the velocity of the piston v_p, that is

$$v_{sf} = \left(\frac{\gamma + 1}{2}\right) v_p \qquad \text{.....(3.5)}$$

where γ is the specific heat ratio.

The temperature of the plasma slug (the layer of shock heated gas particles between the piston and the shock front) is given by

$$T_p = \left(\frac{M}{R_0}\right)\frac{2(\gamma-1)}{(\gamma+1)^2\chi}{v_{sf}}^2 \text{.....(3.6)}$$

where M is the standard atomic weight of the gas heated and χ is the departure coefficient given by

$$\chi = 1 + j\sum_{j=1}^{i}\alpha_j \text{ ... ... (3.7)}$$

for a plasma ionized to *i*th ionized state.

Thus, by using values of axial speed shown in Table 3.1, v_{sf} is calculated using Equation (3.5) and the plasma temperature can be estimated based on Equation (3.6). The specific heat ratio, γ, of argon used is 1.18 with reference to the plot of specific heat ratio, γ of argon as a function of temperature stated by Yong and Tou (1984). Mean while, the departure coefficient, χ used in calculation is 17 by assuming the degree of ionization, α_j is 16 [Yong and Tou, 1984]. The results of the plasma temperature calculation are as shown in Table 3.3 and are plotted in Figure 3.7. The calculation shows that the temperature of the plasma slug increases and attains its maximum value of 97.59 eV at pressure 9.0×10^{-3} mbar, and then decreases to 27.97 eV at 1.8×10^{-2} mbar.

Table 3.3: Calculated plasma temperature at different operating gas pressures

Operating gas pressure (mbar)	Plasma temperature (eV)
9.0×10^{-3}	97.59
1.0×10^{-2}	89.28
1.4×10^{-2}	70.69
1.5×10^{-2}	50.80
1.6×10^{-2}	32.74
1.8×10^{-2}	27.97

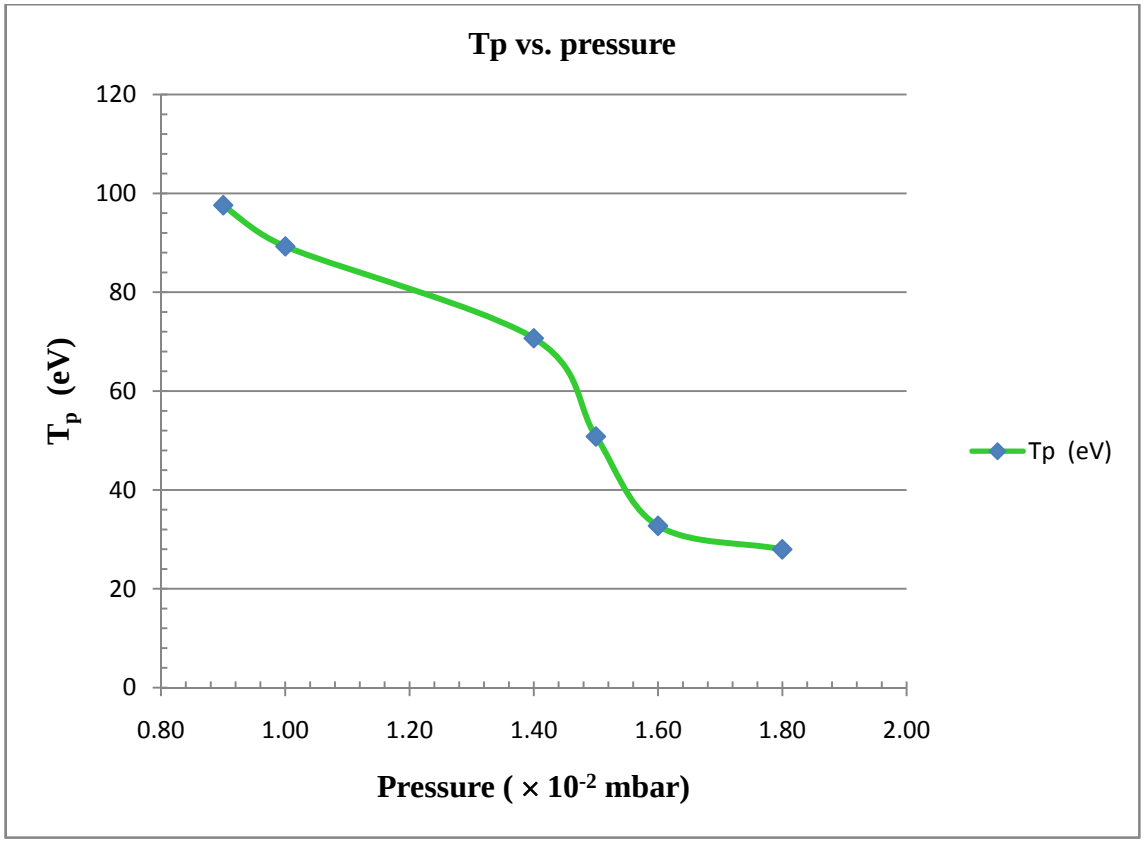

Figure 3.7: Plasma temperature vs. gas pressure